

7. Optimum date range for the observations: 01.11.2020 – 01.03.2021
 Usable range in local sidereal time LST: h – h

Astrophysical context

Present-day stellar abundances are fossil records of the physical conditions of the interstellar medium (ISM) when the stars formed. They indirectly but precisely trace galaxy formation and evolution. In this proposal, we will study the nucleosynthetic signatures found in old stars, in particular the neutron (n)-capture elements ($Z > 30$). They are mainly formed through multiple n-captures, and not through fusion since charged particle reactions beyond Fe are endothermic (except proton captures, responsible for $< 1\%$ of the heavy elements). The n-capture process is split in the *rapid* process (r-process [16, 21]: hosted by neutron star mergers -NSM or supernovae -SN) and the *slow* process (s-process [17]; in AGB or fast rotating massive stars -FRMS) depending on whether the timescale for n-capture is faster or slower than the β -decay [5]. These elements have a complex nucleosynthesis and are not yet deeply investigated as, e.g., α -elements. Unlike the α -elements, all n-capture elements show a large star-to-star abundance scatter (Fig. 1) concealing the contributions from several differing formation processes and sites [13]. Only through precise and accurate abundances we can separate and understand the nature of the sites (e.g., NSM or FRMS) and their chemical yields. Searches for metal-poor stars have almost completely ignored all the stars in the intermediate metallicity range between the very metal-poor stars ($[\text{Fe}/\text{H}] < -2.5$) and disc stars ($[\text{Fe}/\text{H}] > -1.5$). In this region, the number of stars with any measurements of the n-capture elements is tiny, only 20% of the stars according to the sample in the JINA database [1], and only 10% with Eu measurements. According to the metallicity distribution of the Galactic halo 90% of the halo stars are actually in this region [19], with only 10% percent at lower metallicity. Thus an enormous number of halo stars are yet unexplored as far as the abundances of n-capture elements go.

Immediate aim

Our goal is to understand the origin of n-capture elements in the poorly studied part of the halo distribution at $-2.5 < [\text{Fe}/\text{H}] < -1.5$, by observing stars at high resolution and obtaining spectra of $S/N \sim 50$. Our proposal is part of the large collaboration MINCE (Measuring at Intermediate metallicity Neutron-Capture Elements), supported by the COST Action ‘ChETEC’ (<http://www.chetec.eu/>) joining experts in ~ 30 countries. The PI is in charge of the group working on stellar abundances. Investigating the reason for the abundance scatter of n-capture elements is crucial to understanding and answering open questions related to the nature of NSM, magnetic fields of magneto-rotational (MR) SN, size of ^{13}C pockets in AGB stars, and yields from FRMS all in the grand scheme of Galactic chemical evolution (GCE). For such a study, a large, homogeneously analysed sample is crucial. To date, we typically only have abundance information on

Sr, Ba, and possibly Eu in large samples in the range $-2.5 < [\text{Fe}/\text{H}] < -1.5$. Here we will more than quadruple the number of heavy elements that can be used to unveil the nature of the n-capture processes and GCE.

Previous work

The abundance spread is produced by a stochastic process driven by the rarity of the r-process events [2, 7]. The way this dispersion shrinks at higher metallicity constrains the rate of r-process events in the Galactic halo (Fig. 1). Hidden in this region, we can also find signatures of different types of r-process that can have polluted the ISM on different time scales (e.g., [15, 14, 13]). This could be the case if both NSM and MR SNe contributed to the present amount of r-process material [9, 11, 20, 21]. The PI and several Co-Is (beyond the listed) are experts in analysing stellar spectra and deriving abundances of heavy elements, for which we have developed stellar model atmospheres, optimised synthetic spectrum codes (also in 3D [3, 4]) and improved atomic data/line lists (e.g., Th; [12]). On the theoretical side, the collaboration also includes specialists on stellar yields and GCE models (e.g., [10]).

Layout of observations

We will use FEROS to measure abundances in 50 stars, selected from Gaia, RAVE and/or have Strömgren photometry (from which we have T and $[\text{Fe}/\text{H}]$ [18, 6]). The sample stars in the range $8.7 < V < 11.1$, and $[\text{Fe}/\text{H}] \leq -1.5$, $\log g < 3$, so that the observations can be carried out efficiently, yet obtaining $S/N \geq 50$ at 404 nm. Faint targets are sent to larger telescopes. The limit in $\log g$ is set to observe giants, which will allow us to measure more n-capture elements than in dwarfs. We chose stars which have no or little n-capture abundance information available in the literature, and are observable Oct 2020–Apr 2021 (Nov–Mar best). We will accurately measure ~ 20 n-capture elements (Rb, Sr, Y, Zr, Mo, Ru, Ba, La, Ce, Pr, Nd, Sm, Eu, Gd, Tb, Dy, Ho, Os, Pb, Th, see Fig.2 & 3) but also abundances of CNO, Li, Na, Al, Sc and all α - and Fe-peak elements. We plan one additional run to reach the ~ 200 (out of 1000) stars we wish to target with FEROS. Currently, MINCE has been awarded $\sim 10\text{n}$ and has > 150 stars.

Strategic importance for MPIA

Understanding galaxy assembly and evolution are corner stones to MPIA’s Cosmology and Galaxy department. Several research groups (e.g., Bergemann, Rix) focus on the origin of the elements using stellar abundances to explore the chemical enrichment of the Galaxy, by using and developing tools to improve 1D, LTE abundances. In collaboration with groups at MPIA, we will analyse the spectra by deriving stellar parameters and abundances and use 3D, NLTE corrections providing us with a better picture of how and where the heavy n-capture elements formed.

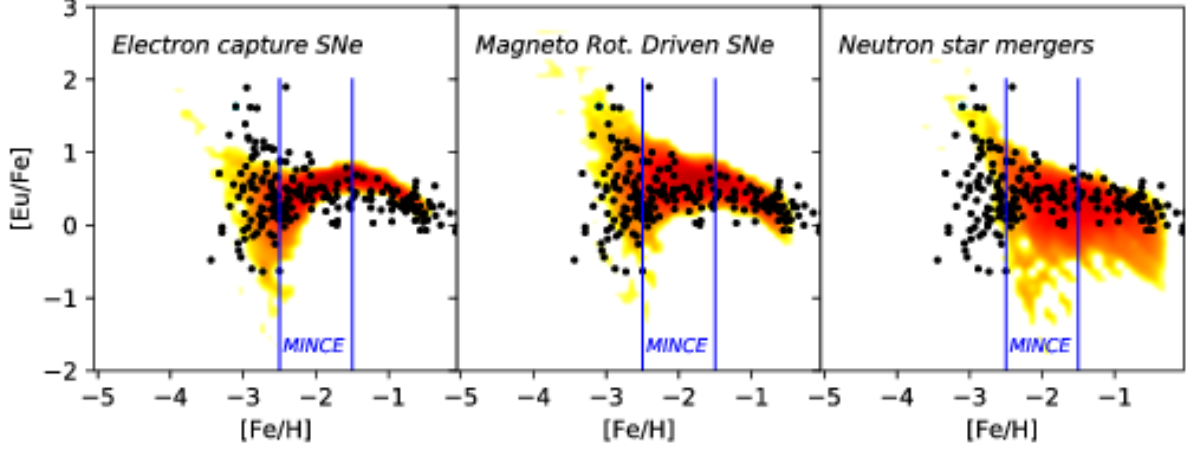


Figure 1: Observed abundance ratios in metal-poor stars compared to Galactic chemical evolution models (adapted from Cescutti & Chiappini 2014, Cescutti et al., 2015). It is striking how few observed data points there are in the metallicity interval $-2.5 \leq [\text{Fe}/\text{H}] \leq -1.5$, compared to those observed at $[\text{Fe}/\text{H}] < -2.5$.

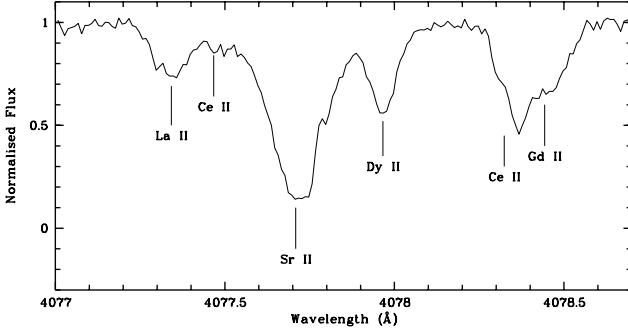


Figure 2: A portion of a SOPHIE spectrum of the metal-poor giant HD 6755 ($T_{\text{eff}} = 5060$, $\log g = 2.7$, $[\text{Fe}/\text{H}] = -1.72$). The high resolution and blue coverage of the FEROS spectrograph allows us to detect lines of many n-capture elements even at a moderate S/N ratio. This spectrum has $S/N \approx 60$ in this region. We aim at a similar S/N ratio (50-60) that will allow us to deblend and analyse weak, blended lines using spectrum synthesis (like the Ce II and Gd II lines in this figure).

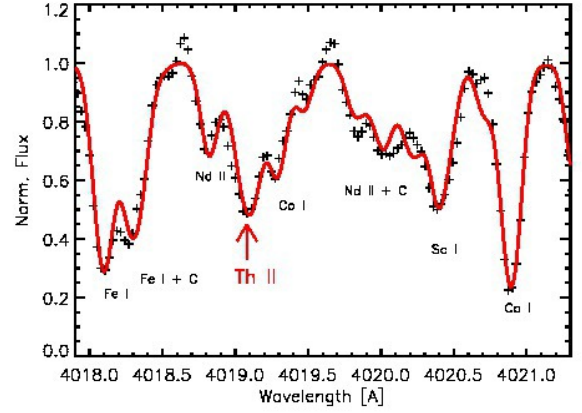


Figure 3: A region around Th in a UVES spectrum of a faint metal-poor ($[\text{Fe}/\text{H}] = -1.81$) giant in the Sagittarius dSph (Sgr J184323). Observations (+) and our best 1D, LTE synthesis on top (red). The high resolution of FEROS and the brightness of our targets allow for detections of many n-capture elements including Th. This spectrum has $S/N \approx 45$ in this region. Figure adapted from Hansen et al. 2018.

9. Objects to be observed

(Objects to be observed with high priority should be marked in last column)

Designation	α (2000)	δ (2000)	magnitude in spectral range to be observed	priority
HD15566	2 ^h 29 ^m 53 ^s .1379	−11° 35′ 10.8959″	8.72000	high
HD7282	1 ^h 12 ^m 6 ^s .30014	−51° 45′ 14.3646″	8.83000	high
HD87064	10 ^h 2 ^m 29 ^s .0879	−8° 3′ 53.9401″	8.97000	high
HD105324	12 ^h 7 ^m 38 ^s .1985	−5° 53′ 10.5995″	9.44600	high
HD270904	4 ^h 57 ^m 41 ^s .7046	−65° 17′ 3.07434″	9.71000	high
CD-51.2403	7 ^h 16 ^m 15 ^s .9396	−51° 35′ 24.8657″	9.92000	high
BD-21.177	1 ^h 7 ^m 59 ^s .4644	−20° 39′ 10.0511″	9.94000	high
673-0956289	3 ^h 12 ^m 16 ^s .7569	−9° 56′ 29.1037″	10.0000	high
BD-00.2101	8 ^h 58 ^m 54 ^s .3052	−1° 5′ 4.14748″	10.0600	high
CD-68.598	8 ^h 55 ^m 27 ^s .5356	−69° 9′ 27.9657″	10.1000	high
BD-20.3039	9 ^h 52 ^m 45 ^s .7516	−21° 17′ 31.9066″	10.1300	high
CD-25.7160	9 ^h 24 ^m 16 ^s .3854	−26° 15′ 19.3565″	10.1500	high
CD-32.8831	12 ^h 38 ^m 29 ^s .0103	−33° 23′ 5.84290″	10.2200	high
CD-24.3687	6 ^h 6 ^m 14 ^s .5960	−24° 41′ 9.91882″	10.2400	high
BD-06.3586	12 ^h 30 ^m 46 ^s .3314	−7° 15′ 50.2728″	10.2600	high
TYC-6654-964-1	11 ^h 19 ^m 21 ^s .2377	−25° 30′ 5.59616″	10.2600	high
TYC-4854-1347-1	8 ^h 6 ^m 19 ^s .7287	−5° 20′ 53.4765″	10.2600	high
BD-07.456	2 ^h 35 ^m 46 ^s .6795	−6° 40′ 47.6491″	10.3900	high
TYC-4699-399-1	2 ^h 45 ^m 29 ^s .0089	−1° 0′ 54.1883″	10.4800	high
TYC-8903-68-1	6 ^h 39 ^m 23 ^s .2416	−64° 40′ 32.2632″	10.4900	high
TYC-4840-159-1	7 ^h 47 ^m 15 ^s .8219	−4° 5′ 46.3097″	10.5500	high
CPD-23.946	5 ^h 52 ^m 12 ^s .6709	−23° 6′ 41.9279″	10.5630	high
BD-05.504	2 ^h 41 ^m 38 ^s .9767	−4° 27′ 35.3478″	10.5740	high
TYC-6471-158-1	4 ^h 48 ^m 47 ^s .8049	−27° 50′ 31.1211″	10.5780	high
CD-35.817	2 ^h 22 ^m 15 ^s .8448	−35° 1′ 1.75690″	10.6000	high
CD-31.8865	11 ^h 14 ^m 23 ^s .1958	−32° 8′ 50.6671″	10.6200	high
BD-18.1229	5 ^h 54 ^m 57 ^s .7592	−18° 29′ 19.4948″	10.7200	high
CD-56.866	4 ^h 12 ^m 45 ^s .5634	−56° 1′ 6.19263″	10.7610	high
TYC-9153-1306-1	4 ^h 11 ^m 0 ^s .424232	−68° 29′ 33.0011″	10.7700	high
TYC-6663-575-1	11 ^h 32 ^m 52 ^s .9797	−29° 13′ 13.7759″	10.7730	high
HD274816	5 ^h 24 ^m 49 ^s .1453	−48° 52′ 29.1074″	10.7880	high
TYC-6103-778-1	12 ^h 29 ^m 36 ^s .7330	−16° 59′ 32.8020″	10.8200	high
TYC-8026-382-1	0 ^h 20 ^m 28 ^s .0966	−47° 54′ 24.2029″	10.8200	high
TYC-6059-916-1	10 ^h 13 ^m 51 ^s .3217	−15° 2′ 20.4121″	10.8300	high
CD-30.9667	12 ^h 6 ^m 13 ^s .4390	−31° 39′ 43.0925″	10.8400	high
TYC-5841-1251-1	0 ^h 2 ^m 34 ^s .3168	−19° 24′ 59.0982″	10.8800	high
TYC-7055-458-1	5 ^h 27 ^m 27 ^s .8411	−30° 56′ 23.2054″	10.8950	high
CD-36.2184	5 ^h 20 ^m 43 ^s .1957	−36° 17′ 59.7226″	10.9100	high
TYC-5532-1432-1	12 ^h 23 ^m 32 ^s .4264	−14° 31′ 10.6078″	10.9100	high
TYC-8866-463-1	3 ^h 14 ^m 55 ^s .0828	−66° 56′ 59.1376″	10.9280	high
TYC-7034-241-1	3 ^h 40 ^m 3 ^s .64975	−37° 25′ 18.3792″	10.9680	high
TYC-5310-259-1	3 ^h 44 ^m 53 ^s .0219	−13° 56′ 10.6295″	10.9710	high
TYC-5913-127-1	5 ^h 5 ^m 50 ^s .5428	−21° 45′ 7.93762″	11.0000	high
CD-26.786	2 ^h 11 ^m 19 ^s .3782	−25° 38′ 40.9991″	11.0000	high
TYC-8026-743-1	0 ^h 22 ^m 32 ^s .2845	−48° 39′ 45.0769″	11.0590	high
CD-31.8044	10 ^h 12 ^m 19 ^s .6339	−32° 21′ 34.7113″	11.0700	high
TYC-6104-691-1	12 ^h 39 ^m 2 ^s .26456	−16° 14′ 50.2840″	11.0900	high
TYC-6434-624-1	2 ^h 34 ^m 56 ^s .9106	−24° 29′ 1.95786″	11.0900	high
List truncated				

10. Justification of the amount of observing time requested:

As we target heavy elements with weak lines located in the blue spectral range, we need high-resolution spectra that allow for precise and accurate abundance determinations. A careful spectrum synthesis is needed to deblend the convolved line profiles. Most n-capture element transitions are located (only) in the blue ($< 450\text{nm}$ [100, 101]), and we therefore need a spectrograph such as FEROS that covers this region (down to 350nm). At a SNR of ~ 50 we can derive abundances of up to 20 n-capture elements (see Figs. 2 and 3). In order to achieve this SNR we use the FEROS ETC V.106.1 with the following observing conditions: airmass = 1.5, seeing=1.3, fast readout and 1x1 binning, and gray Moon constraint since we pursue fairly bright targets with FEROS ($V_{\text{mag}} \leq 11$). For exposure time estimates we used Moon FLI=0.6. Most of our targets are giants (typically of 4500K), but stars with cooler temperatures prolong the observations slightly (by $\sim 100 - 200\text{sec}$ depending on magnitude).

Representative examples are listed below:

$V_{\text{mag}}=9.0$, $T=4500\text{K}$ (4000K), $404\text{nm}/\text{order } 55$, $\text{SNR} \sim 50$ after 400 (500)sec

$V_{\text{mag}}=10.0$, $T=4500\text{K}$ (4000K), $404\text{nm}/\text{order } 55$, $\text{SNR} \sim 50$ after 900 (1100)sec

$V_{\text{mag}}=11.0$, $T=4500\text{K}$, $404\text{nm}/\text{order } 55$, $\text{SNR} \sim 50$ after 2100sec

The listed exposure times do **not** include overhead.

The stars are normal, cool, low-mass stars and do not require special calibrations or very accurate radial velocities, so we request day calibrations (bias, flat fields, wavelength calibrations etc.). Following the manual, this results in $\sim 8\text{min}$ overhead per exposure. However, following the previous run, we reduced this time to $\sim 4\text{min}$ overhead. Each target will be exposed for less than one hour resulting in $\sim 71400\text{sec}$ **on targets** + $\sim 12000\text{sec}$ **overhead** ~ 23.3 **hours in total**.

If back-up targets are needed, we have ~ 100 targets from the past period (which were not observed due to COVID-19) in place that can be used as fillers in case of e.g., strong winds from a given direction.

Since our targets spread a range in RA, service mode might be better suited. However, with the observing experience within the MINCE team, we are fully capable of carrying out the observations ourselves (which can be done in $\sim 3\text{n}$).

11. Constraints for scheduling observations for this application:

12. Observational experience of observer(s) named under 2.3:

(at least one observer must have sufficient experience)

Apr 2013 – HDS/Subaru, Mauna Kea, Hawaii, US: Co-I (1n $\sim 10\text{h}$ - visitor mode)

Aug 2010 – X-Shooter/VLT ESO, Chile: Co-I (1.5n $\sim 15\text{h}$ - visitor mode)

Jul 2006 – AURELIE/OHP, Observatoire de Haute Provence, France: Co-I (5n - visitor mode)

2004 – Brorfelde Schmidt telescope, Brorfelde Observatory, Denmark: Co-I (1n - visitor mode)

Mar 2020 – UVES/VLT ESO, Chile: PI (2n - visitor mode)

2008 - 2020 – High-resolution spectroscopy, world wide including PEPSI: PI or Co-I - $> 200\text{h}$ service mode

The Co-observer (M. Hanke) will by 2020 have $>14\text{n}$ of FEROS observing experience and 2n of UVES/VLT time.

13. Observing runs at the ESO 2.2m-telescope (preferably during the last 3 years) and publications resulting from these

Telescope	instrument	date	hours	success rate	publications
2.2m	FEROS	Jan 20	15	$\sim 100\%$	Analysis in progress

14. References for items 8 and 13:

- [1] Abomalima, A., & Frebel, A. 2018, *ApJS*, 238, 36
- [2] Argast, D., Samland, M., Thielemann, F.-K., et al. 2004, *A&A*, 416, 997
- [3] Bonifacio, P., Caffau, E., Ludwig, H.-G., et al. 2018, *A&A*, 611, A68
- [4] Bonifacio, P., Caffau, E., Spite, M., et al. 2018, *A&A*, 612, A65
- [5] Burbidge, E. M., Burbidge, G. R., Fowler, W. A., et al. 1957, *RvMP*, 29, 547
- [6] Casagrande, L., Silva Aguirre, V., Stello, D., et al. 2014, *ApJ*, 787, 110
- [7] Cescutti, G. 2008, *A&A*, 481, 691
- [8] Cescutti, G., Chiappini, C. 2014, *A&A*, 565, A51
- [9] Cescutti, G., Romano, D., Matteucci, F., et al. 2015, *A&A*, 577, A139
- [10] Cescutti, G., Hirschi, R., Nishimura, N., et al. 2018, *MNRAS*, 478, 4101
- [11] Côté, B., Fryer, C. L., Belczynski, K., et al. 2018, *ApJ*, 855, 99
- [12] Hansen, C. J., El-Souri, M., Monaco, L., et al. 2018, *ApJ*, 855, 83
- [13] Hansen, C. J., Montes, F., & Arcones, A. 2014, *ApJ*, 797, 123
- [14] Hansen, C. J., Andersen, A. C., & Christlieb, N. 2014, *A&A*, 568, A47
- [15] Hansen, C. J., Primas, F., Hartman, H., et al. 2012, *A&A*, 545, A31
- [16] Horowitz, C. J., Arcones, A., Côté, B., et al. 2018, *arXiv:1805.04637*
- [17] Käppeler, F., Gallino, R., Bisterzo, S., & Aoki, W. 2011, *Reviews of Modern Physics*, 83, 157
- [18] Paunzen, E., 2015, *A&A*, 580, 23
- [19] Schörck, T., Christlieb, N., Cohen, J. G., et al. 2009 *A&A*, 507, 817
- [20] Simonetti, P., Matteucci, F., Greggio, L., et al. 2019, *MNRAS*, 486, 2896
- [21] Watson, D., Hansen, C. J., Selsing, J., et al. 2019, *Nature*, 574, 497
- [100] Sneden, C., Cowan, J. J., Lawler, J. E., et al. 2003, *ApJ*, 591, 936
- [101] Hansen, C. J., Ludwig, H.-G., Seifert, W., et al. 2015, *Astronomische Nachrichten*, 336, 665

Tolerance limits for planned observations:

maximum seeing:	1.3''	minimum transparency:	%	maximum airmass:	1.5
photometric conditions:	no	moon: max. phase / \angle :	/ $^{\circ}$	min. / max. lag:	/ nights